

Miniature spectrometer and beam splitter for an optical coherence tomography on a silicon chip

B. I. Akca,^{1,*} B. Považay,² A. Alex,² K. Wörhoff,¹ R. M. de Ridder,¹ W. Drexler,² and M. Pollnau¹

¹Integrated Optical MicroSystems Group, MESA + Institute for Nanotechnology, University of Twente, 7500 AE Enschede, The Netherlands

²Center for Medical Physics and Biomedical Engineering, Medical University of Vienna, General Hospital Vienna, 4L, Währinger Gürtel 18-20, A-1090 Vienna, Austria

*bavci@partners.org

Abstract: Optical coherence tomography (OCT) has enabled clinical applications that revolutionized *in vivo* medical diagnostics. Nevertheless, its current limitations owing to cost, size, complexity, and the need for accurate alignment must be overcome by radically novel approaches. Exploiting integrated optics, we assemble the central components of a spectral-domain OCT system on a silicon chip. The spectrometer comprises an arrayed-waveguide grating with 136-nm free spectral range and 0.21-nm wavelength resolution. The beam splitter is realized by a non-uniform adiabatic coupler with its 3-dB splitting ratio being nearly constant over 150 nm. With this device whose overall volume is 0.36 cm³ we demonstrate high-quality *in vivo* imaging in human skin with 1.4-mm penetration depth, 7.5-μm axial resolution, and a signal-to-noise ratio of 74 dB. Considering the reasonable performance of this early OCT on-a-chip system and the anticipated improvements in this technology, a completely different range of devices and new fields of applications may become feasible.

©2013 Optical Society of America

OCIS codes: (170.4500) Optical coherence tomography; (230.3120) Integrated optics devices.

References and links

1. D. Huang, E. A. Swanson, C. P. Lin, J. S. Schuman, W. G. Stinson, W. Chang, M. R. Hee, T. Flotte, K. Gregory, C. A. Puliafito, and J. G. Fujimoto, "Optical coherence tomography," *Science* **254**(5035), 1178–1181 (1991).
2. A. F. Fercher, "Optical coherence tomography - development, principles, applications," *Z. Med. Phys.* **20**(4), 251–276 (2010).
3. D. Culemann, A. Knuettel, and E. Voges, "Integrated optical sensor in glass for optical coherence tomography," *IEEE J. Sel. Top. Quantum Electron.* **6**(5), 730–734 (2000).
4. E. Margallo-Balbás, M. Geljon, G. Pandraud, and P. J. French, "Miniature 10 kHz thermo-optic delay line in silicon," *Opt. Lett.* **35**(23), 4027–4029 (2010).
5. G. Yurtsever, P. Dumon, W. Bogaerts, and R. Baets, "Integrated photonic circuit in silicon on insulator for Fourier domain optical coherence tomography," *Proc. SPIE* **7554**, 75541B (2010).
6. M. K. Smit, "New focusing and dispersive planar component based on an optical phased array," *Electron. Lett.* **24**(7), 385–386 (1988).
7. D. Choi, H. Hiro-Oka, H. Furukawa, R. Yoshimura, M. Nakanishi, K. Shimizu, and K. Ohbayashi, "Fourier domain optical coherence tomography using optical demultiplexers imaging at 60,000,000 lines/s," *Opt. Lett.* **33**(12), 1318–1320 (2008).
8. D. H. Choi, H. Hiro-Oka, K. Shimizu, and K. Ohbayashi, "Spectral domain optical coherence tomography of multi-MHz A-scan rates at 1310 nm range and real-time 4D-display up to 41 volumes/second," *Biomed. Opt. Express* **3**(12), 3067–3086 (2012).
9. Y. Jiao, B. W. Tilma, J. Kotani, R. Nötzel, M. K. Smit, S. He, and E. A. Bente, "InAs/InP(100) quantum dot waveguide photodetectors for swept-source optical coherence tomography around 1.7 μm," *Opt. Express* **20**(4), 3675–3692 (2012).
10. B. W. Tilma, Y. Jiao, J. Kotani, E. Smalbrugge, H. P. M. M. Ambrosius, P. J. Thijs, X. J. M. Leijten, R. Nötzel, M. K. Smit, and E. A. J. M. Bente, "Integrated tunable quantum-dot laser for optical coherence tomography in the 1.7 μm wavelength region," *IEEE J. Quantum Electron.* **48**(2), 87–98 (2012).
11. B. I. Akca, V. D. Nguyen, J. Kalkman, N. Ismail, G. Sengo, F. Sun, T. G. van Leeuwen, A. Driessen, M. Pollnau, K. Wörhoff, and R. M. de Ridder, "Toward spectral-domain optical coherence tomography on a chip," *IEEE J. Sel. Top. Quantum Electron.* **18**(3), 1223–1233 (2012).

12. V. D. Nguyen, B. I. Akca, K. Wörhoff, R. M. de Ridder, M. Pollnau, T. G. van Leeuwen, and J. Kalkman, "Spectral domain optical coherence tomography imaging with an integrated optics spectrometer," *Opt. Lett.* **36**(7), 1293–1295 (2011).
13. B. I. Akca, L. Chang, G. Sengo, K. Wörhoff, R. M. de Ridder, and M. Pollnau, "Polarization-independent enhanced-resolution arrayed-waveguide grating used in spectral-domain optical low-coherence reflectometry," *IEEE Photon. Technol. Lett.* **24**, 848–850 (2012).
14. V. D. Nguyen, N. Weiss, W. Beeker, M. Hoekman, A. Leinse, R. G. Heideman, T. G. van Leeuwen, and J. Kalkman, "Integrated-optics-based swept-source optical coherence tomography," *Opt. Lett.* **37**(23), 4820–4822 (2012).
15. K. Wörhoff, E. J. Klein, M. G. Hussein, and A. Driessen, "Silicon oxynitride based photonics," in *Proceedings of IEEE International Conference on Transparent Optical Networks* (IEEE, 2008), pp. 266–269.
16. W. H. Louisell, "Analysis of the single tapered mode coupler," *Bell Syst. Tech. J.* **33**, 853–870 (1955).
17. M. K. Smit and C. van Dam, "PHASAR-based WDM-devices: Principles, design and applications," *IEEE J. Sel. Top. Quantum Electron.* **2**(2), 236–250 (1996).
18. C. M. Sparrow, "On spectroscopic resolving power," *Astrophys. J.* **44**, 76–86 (1916).
19. H. Takahashi, S. Suzuki, K. Kato, and I. Nishi, "Arrayed-waveguide grating for wavelength division multi/demultiplexer with nanometer resolution," *Electron. Lett.* **26**(2), 87–88 (1990).
20. Z. Hu, Y. Pan, and A. M. Rollins, "Analytical model of spectrometer-based two-beam spectral interferometry," *Appl. Opt.* **46**(35), 8499–8505 (2007).
21. K. Takada, H. Yamada, and K. Okamoto, "320-channel multiplexer consisting of a 100 GHz-spaced parent AWG and 10 GHz-spaced subsidiary AWGs," *Electron. Lett.* **35**(10), 824–826 (1999).
22. B. I. Akca, C. R. Doerr, G. Sengo, K. Wörhoff, M. Pollnau, and R. M. de Ridder, "Broad-spectral-range synchronized flat-top arrayed-waveguide grating applied in a 225-channel cascaded spectrometer," *Opt. Express* **20**(16), 18313–18318 (2012).
23. B. Hofer, B. Povazay, B. Hermann, A. Unterhuber, G. Matz, and W. Drexler, "Dispersion encoded full range frequency domain optical coherence tomography," *Opt. Express* **17**(1), 7–24 (2009).
24. E. Fuchs and S. Raghavan, "Getting under the skin of epidermal morphogenesis," *Nat. Rev. Genet.* **3**(3), 199–209 (2002).
25. A. Alex, B. Povazay, B. Hofer, S. Popov, C. Glittenberg, S. Binder, and W. Drexler, "Multispectral in vivo three-dimensional optical coherence tomography of human skin," *J. Biomed. Opt.* **15**(2), 026025 (2010).
26. J. A. Izatt and M. A. Choma, "Theory of optical coherence tomography," in *Optical Coherence Tomography: Technology and Applications*, W. Drexler and J. G. Fujimoto, eds. (Springer, Berlin, New York, 2008), pp. 47–72.
27. M. M. Spühler, B. J. Offrein, G. Bona, R. Germann, I. Massarek, and D. Erni, "A very short planar silica spot-size converter using a nonperiodic segmented waveguide," *J. Lightwave Technol.* **16**(9), 1680–1685 (1998).
28. O. Mitomi, K. Kasaya, and H. Miyazawa, "Design of a single-mode tapered waveguide for low-loss chip-to-fiber coupling," *IEEE J. Quantum Electron.* **30**(8), 1787–1793 (1994).
29. A. Sugita, A. Kaneko, K. Okamoto, M. Itoh, A. Himeno, and Y. Ohmori, "Very low insertion loss arrayed-waveguide grating with vertically tapered waveguides," *IEEE Photon. Technol. Lett.* **12**(9), 1180–1182 (2000).

1. Introduction

Optical coherence tomography (OCT) is a well-established optical technique in the medical sciences for acquiring micrometer-scale-resolution cross-sectional images of specimen in a non-invasive way [1]. State-of-the-art OCT systems operate in the frequency domain, either with a broad-band light source and a spectrometer, called "spectral-domain OCT" (SD-OCT), or with a rapidly wavelength-tuned laser, called "swept-source OCT" (SS-OCT) [2]. Both systems typically contain a combination of fiber and free-space components which add to the instrument size and cost, affect its mechanical stability, and therefore require active alignment. Integrating several complex optical devices as miniaturized components on a single microchip improves mechanical stability for maintenance-free operation and accesses lithographic high-volume fabrication for dramatic cost reduction and improved repeatability. Integrated systems hold promise for wider deployment of OCT technology and open new fields of applications. Despite these opportunities, OCT based upon integrated optical components has as yet yielded only preliminary results. For time-domain OCT, a microchip integrating eight parallel Michelson interferometers was demonstrated [3]; also a rapid scanning delay line with a 10-kHz line rate and 1-mm scan range was realized [4]. A Michelson interferometer for an SS-OCT system was demonstrated with an insufficient 40- μm axial resolution and 25-dB sensitivity [5]. SD-OCT imaging was achieved with an arrayed-waveguide-grating (AWG) spectrometer [6]; however, sensitivity had to be boosted by semiconductor optical amplifiers [7,8]. InAs/InP quantum-dot-based waveguide photodetectors and a tunable laser source for SS-OCT systems operating around 1.7 μm were presented [9,10], but OCT imaging was not reported. We demonstrated SD-OCT cross-

sectional imaging of a multilayered phantom with an AWG [11,12] and improved its in-depth detection range toward the level of existing bulk optical systems [13]. Recently, a combination of Michelson interferometer, reference arm, and directional coupler for balanced detection demonstrated SS-OCT of a phantom with an 80-dB sensitivity and 5-mm depth range in air [14].

Here we present an important step toward a cheap, compact, and maintenance-free SD-OCT system by integrating its central components, the beam splitter and spectrometer, on a silicon chip [Fig. 1(a)]. With this device whose overall volume is 0.36 cm^3 which is significantly (\sim two orders of magnitude) smaller compared to bulky counterparts (spectrometer and splitter) we demonstrate *in vivo* imaging in human skin, delivering averaged cross-sections of sufficient quality for medical diagnosis. Integrated optics holds a great promise for mass-produced OCT systems with significantly reduced costs and smaller footprints which can make them affordable and accessible for wider groups of researchers.

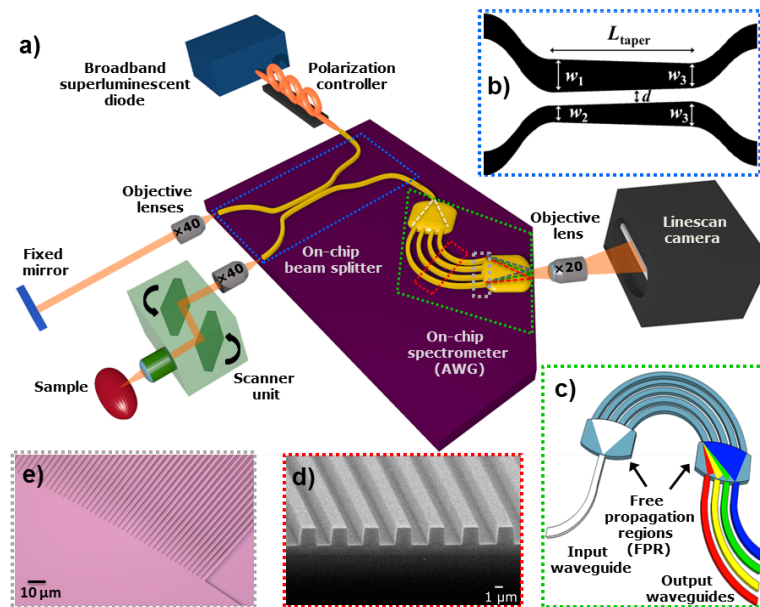


Fig. 1. Schematic of the partially integrated SD-OCT system. (a) The complete SD-OCT set-up comprising a broadband light source, the microchip with its optical circuitry consisting of a broadband beam splitter and the spectrometer (purple plate, magnified for viewing purposes), line-scan camera, and reference and sample arms, the latter including a scanner unit. (b) Details of the integrated broadband beam splitter, a 3-dB non-uniform adiabatic coupler with specific waveguide widths of $w_1 = 2 \mu\text{m}$, $w_2 = 1.8 \mu\text{m}$, $w_3 = 1.6 \mu\text{m}$, a waveguide separation of $d = 0.8 \mu\text{m}$, and a taper length of $L_{\text{taper}} = 3.5 \text{ mm}$. (c) A conventional AWG which, in contrast to our device, includes output channels. (d) Scanning electron microscope image of the arrayed-waveguide section of the AWG before top-cladding deposition. (e) Optical microscope image of linear tapers at the waveguide/FPR interface of the fabricated AWG spectrometer.

2. Design, fabrication, and characterization

2.1 Microchip fabrication

The integrated components, coupler and AWG, were realized in silicon oxynitride (SiON) [15]. An 8- μm -thick oxide layer was thermally grown onto a 100-mm-diameter, $\langle 100 \rangle$ oriented silicon substrate. A SiON layer was deposited in an Oxford Plasmalab System 133 plasma-enhanced chemical vapor deposition (PECVD) reactor at 300°C substrate temperature, 60 W power (187.5 kHz), and 500 mTorr chamber pressure. Silane (2% SiH_4 diluted in N_2) and N_2O served as precursors, with a relative gas-flow ratio $\text{N}_2\text{O}/\text{SiH}_4$ of 0.58, followed by thermal annealing at 1150°C for 3 h. A 500-nm-thick photoresist layer was spin-

coated and patterned by standard lithography and a development step. Single-mode channel waveguides with a 1.8- μm width, 1- μm height, 1.54 core refractive index, and 1.4485 cladding refractive index, enabling bending radii down to 0.5 mm, were etched in a Plasma Therm 790 reactive-ion etching reactor applying a CHF_3/O_2 gas mixture (100 sccm / 2 sccm) at 28 mTorr pressure, 350 W plasma power, and 20°C substrate temperature. After removing the photoresist, growth of a 1- μm -thick oxide layer by low-pressure chemical vapor deposition using tetraethyl orthosilicate as precursor and a 3- μm -thick PECVD oxide layer were each followed by thermal annealing at 1150°C for 3 h. The device size is $3.0 \times 1.2 \times 0.1 \text{ cm}^3$.

2.2 Broadband non-uniform adiabatic coupler

A directional coupler, consisting of two coupled parallel uniform waveguides, exhibits a wavelength-dependent coupling ratio [Fig. 2(a), “uniform”], making it unsuitable for use as an integrated beam splitter in broad-band OCT applications. This wavelength dependence can be significantly reduced by use of a non-uniform adiabatic coupler with linearly tapered waveguides [16], see Fig. 1(b). At their input, both the fundamental (even) and first-order (odd) mode of the composite structure are excited by light from either of the two isolated waveguides. If the propagation constants of the isolated waveguides are sufficiently different, the power in each of them predominantly couples to only one system mode.

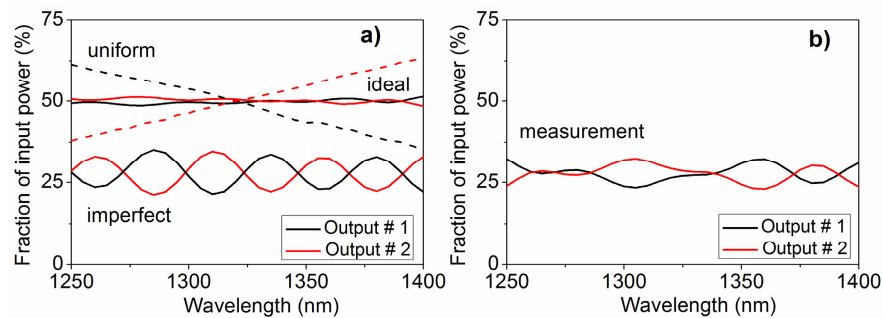


Fig. 2. Wavelength dependence of the integrated beam splitter. **(a)** Simulated transmission of a uniform, i.e., intrinsically highly wavelength-dependent coupler (dashed lines) and the non-uniform adiabatic coupler in the ideal case, i.e., without fabrication imperfections, and including incomplete etching of the SiON layer in the gap region. **(b)** Measured transmission of the fabricated non-uniform adiabatic coupler. An oscillatory behavior can be observed, with an excess loss of 2.5 dB.

We designed a linearly tapered directional coupler [Fig. 1(b)]. The coupler was simulated as a two-dimensional five-layer slab using the beam propagation method (Phoenix, OptoDesigner), showing a weak wavelength dependence over a range larger than 150 nm [Fig. 2(a), “ideal”]. In the straight coupler section, the waveguides were tapered adiabatically, resulting in negligible power conversion between the system modes, from $w_1 = 2 \text{ }\mu\text{m}$ down to $w_3 = 1.8 \text{ }\mu\text{m}$ and from $w_2 = 1.6 \text{ }\mu\text{m}$ up to $w_3 = 1.8 \text{ }\mu\text{m}$, respectively, over a length of $L_{\text{taper}} = 3.5 \text{ mm}$. The gap between waveguides was $d = 0.8 \text{ }\mu\text{m}$.

TE-polarized light from a supercontinuum source (Fianium SC450) was coupled to the input waveguide of the fabricated coupler by a polarization-maintaining single-mode fiber. The output signal was fiber-coupled to an optical spectrum analyzer (iHR 550, Horiba Jobin Yvon) and analyzed. To eliminate fiber-to-chip coupling losses, the transmission response was normalized to a straight waveguide. The fabricated coupler showed a coupling ratio exhibiting an oscillatory wavelength dependence with a splitting ratio of $\pm 1.76 \text{ dB}$ and 2.5 dB excess loss [Fig. 2(b)], evoked by incomplete etching of the gap between the waveguides. Simulation of this fabrication error qualitatively reproduced this behavior [Fig. 2(a), “imperfect”]. Since the light fractions traveling via the reference and sample arm both pass twice through the coupler, once in “cross”- and once in “bar”-direction, the ripple in the

splitting ratio results in a variation of the signal strength over the full bandwidth of < 0.2 dB at the detector array.

2.3 Arrayed-waveguide grating for enhanced depth range

In an AWG spectrometer light from an input waveguide horizontally diverges in a planar-waveguide free-propagation region (FPR) and illuminates the input facets of a number M of arrayed waveguides [Fig. 1(c)]. A constant path-length increment ΔL between adjacent arrayed waveguides causes a phase gradient across their outputs, depending linearly on frequency. These outputs, arranged on a circle, excite approximately cylindrical wavefronts in the second FPR, focusing different wavelengths onto different output waveguides. As the integrated spectrometer of the miniaturized SD-OCT system, an AWG operating at a center wavelength of $\lambda_c^{AWG} = 1250$ nm, with a large FSR of 136 nm and a high overall wavelength resolution of $\delta\lambda = 0.21$ nm was designed by choosing [17] a grating order $m = 9$ and $\Delta L = 7.6$ μm . Linear tapers at the waveguide/FPR interfaces [Fig. 1(e)] diminish the excess loss to 1.5 dB. A scanning electron microscope image of the arrayed waveguides before the top oxide deposition is shown in Fig. 1(d).

The depth detection range in SD-OCT is limited by the wavelength resolution of its spectrometer [2]. In conventional AWGs [Fig. 1(c)] this resolution is determined by the number of output channels, i.e. sampling points, which is typically limited to a few hundreds [6]. By imaging the AWG output focal plane directly onto a camera [Fig. 1(a)], the number of sampling points increases to the number of camera pixels that are addressed. In this way the additional signal roll-off due to discretely located output channels of the AWG spectrometer can be eliminated [11]. The overall spectral resolution of the imaging system is given as the combination of the detector-limited and the arrayed-waveguide-limited resolution [13]. With a $\times 20$ objective lens the usable light-source bandwidth of 75 nm, centered at $\lambda_c^{Source} \sim 1320$ nm, was imaged onto the entire 1024 detector pixels, resulting in a wavelength spacing of 0.073 nm/pixel. Combined with the Sparrow-criterion-based arrayed-waveguide-limited resolution [18,19] of $\Delta\lambda = \lambda_c^{AWG}/1.26Mm = 0.22$ nm, where $M = 510$, the overall spectral resolution [20] was calculated as $\delta\lambda = 0.225$ nm, theoretically resulting in a depth range of 1.9 mm in air, as compared to 0.5 mm with output channels. The free spectral range (FSR) can be extended and simultaneously $\delta\lambda$ enhanced by cascading several AWGs [21,22], thereby significantly improving the axial resolution and depth range in OCT.

3. OCT Performance

3.1 Partially integrated SD-OCT system

A schematic of the SD-OCT system is shown in Fig. 1(a). Partially polarized light from a broadband superluminescent diode (Previum, Thorlabs) with a 1320-nm center wavelength, full-width-at-half-maximum bandwidth of 100 nm, and a fiber-coupled optical power of 5.5 mW was launched via a butt-coupled fiber into one arm of the directional coupler, delivering approximately 0.5 mW to both, the reference and sample arm. Light polarization was adjusted to maximize the interference signal at the detector. Light exiting the reference and sample arms was collimated by $\times 40$ objective lenses with a numerical aperture (NA) of 0.65 and directed toward reference mirror and sample, respectively. The signal-to-noise ratio (SNR), axial resolution, and imaging range were measured by placing a mirror in the sample arm, which was moved for depth-ranging measurements. Returning light was focused by the respective objective lenses into the waveguides and passed through the coupler to the AWG. Its output was imaged by a $\times 20$ objective lens (NA = 0.40) onto the entire, 2.5-mm-wide array of an infrared linescan camera (SUI1024-LDH-1.7RT-0500/LC, 1024 pixels, 25×500 μm^2 pixel size, Goodrich) with a magnification factor of $\sim 10:1$. The axial (depth- or A-) scan rate of the OCT system was 47 kHz, corresponding to a frame rate of 46 Hz with 1024 A-scans (each 1024 pixels) per frame. For *in vivo* imaging the sample arm consisted of a scanner unit with a close pair of galvanometric mirrors for scanning in two dimensions and a telecentric scan lens (LSM03-BB, Thorlabs) covered by a closed patient interface for direct

contact via a 10°-tilted, 4-mm-thick sapphire window to avoid specular reflections from the air/tissue interface. The lateral resolution was limited by the NA of the scan lens and the incident beam size to 20 μm . The mirror deflection was controlled by a field-programmable gate array triggered by the camera output. Digital data were transferred from the camera to a frame grabber (NI-1429, National Instruments) by a high-speed CameraLink connection. A Labview programming interface (National Instruments) was employed for detection, control, and real-time display. The k -mapping and dispersion-compensating procedures were previously explained [23]. The option for full-range decoding was not activated.

The integrated device was interfaced to the light source, external reference arm, two-dimensional scanning system, and linescan camera [Fig. 1(a)] and the system performance was analyzed. The SNR, axial resolution, and imaging range were measured by placing a mirror in the sample arm, which was moved for depth-ranging measurements. An in-tissue depth range of 1.4 mm and axial resolution of 7.5 μm was achieved. Close to the zero delay where both interferometer arms are equal in length, a SNR of 74 dB was measured for 0.5 mW of optical power on the sample.

3.2 *In vivo* imaging with a partially integrated OCT system

The feasibility of on-chip OCT was demonstrated by *in vivo* imaging of human skin above the proximal interphalangeal joint of the middle finger by applying contact gel to the imaging sites as an index-matching medium to decrease the surface reflectivity. The averaged *en-face* and corresponding cross-sectional tomograms are shown in Fig. 3, with corresponding regions indicated by colored marks or dashed lines, respectively. The morphology of several layers including the stratum corneum and uncornified layers of the epidermis [Fig. 3(a)], stratum papillare and reticulare of the dermis [Fig. 3(b)], and deeper dermis featuring vessels [Fig. 3(c)] has been visualized within a 1.4-mm depth range, sufficient for performing diagnostic procedures due to the fact that most skin malignancies are of epidermal origin [24]. In pigmented thin skin (Fig. 4), additionally to their bright appearance in OCT above the skin, hairs are identified as dark, almost vertical channels. The layered structure of the pigmented thin skin is well visualized throughout the cross-sectional series and a three-dimensional volume-rendered representation is depicted in Fig. 4(e).

3.3 Performance comparison of on-chip with bulk system

Performance of the partially integrated system was compared to a 1320-nm fiber-based, custom-designed SD-OCT system [25] with a conventional spectrometer by acquiring OCT images of scar tissue utilizing the same light source, detection system, patient interface, sample, and processing method (Fig. 5). The axial resolution of the fiber-based system was ~ 5.7 μm in tissue, slightly better than the 7.5- μm resolution of the on-chip system. However, the 74-dB SNR of the on-chip system lags behind the 94-dB value of the fiber-based system. The theoretical shot-noise-limited SNR [26] of both devices is 107 dB due to the shared camera with $>70\%$ quantum efficiency and 13.9 μs exposure time at 0.5 mW optical power incident on the sample. Figure 5(a) shows the OCT image taken with $32 \times$ averages using the fiber-based system. The zero delay of the on-chip system was offset by ~ 800 μm toward the region of interest to compensate for ~ 10 dB loss caused by signal roll-off. The resulting OCT image, also taken with $32 \times$ averages, is shown in Fig. 5(b). A signal roll-off of 16 dB was measured at 1.4 mm depth range. The signal roll-off curves obtained by measuring the signal strength of a known reflector at different locations of the on-chip (blue dashed line) and fiber-based (black solid line) system are compared in Fig. 5(c). The resulting effective signal roll-off of the on-chip system after compensation, i.e., shifting its zero delay by ~ 800 μm and averaging of 32 frames (blue solid line), comes close to the signal roll-off of the fiber-based system.

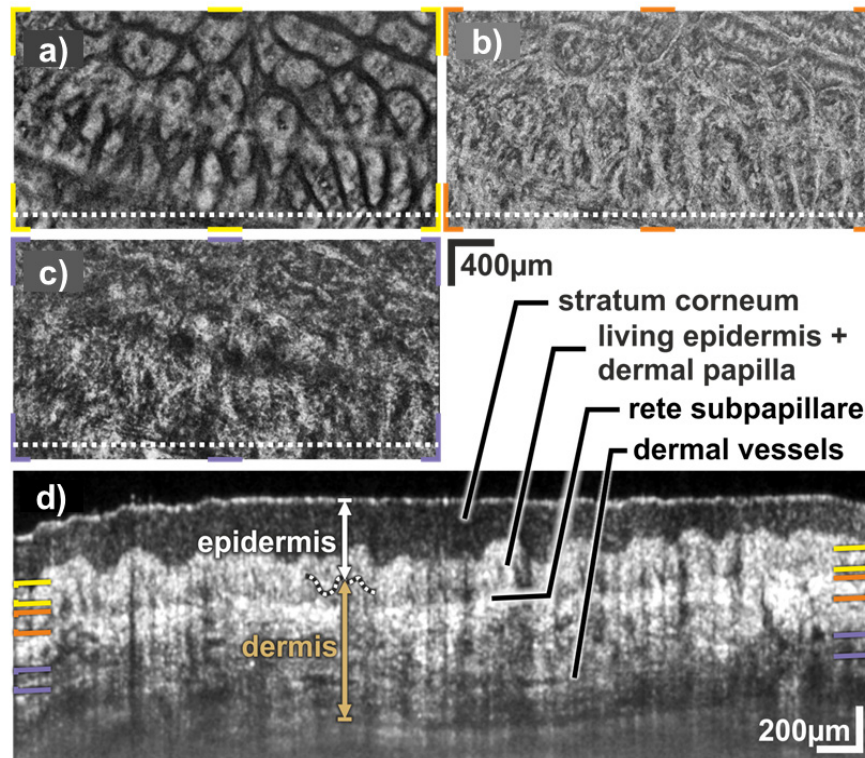


Fig. 3. Images of glabrous skin at interdigital joint taken using the partially integrated SD-OCT system. *En face* section at (a) the deeper epidermal layers featuring the living epidermis on top of the dermal papillae (yellow), (b) rete subpapillare where fibrous components dominate the basis of the dermal papillae (orange) and (c) the deeper dermis with vessels (violet). (d) Cross-section as indicated by the dotted white line in the *en face* sections. Colored indicators depict the location of the *en face* views.

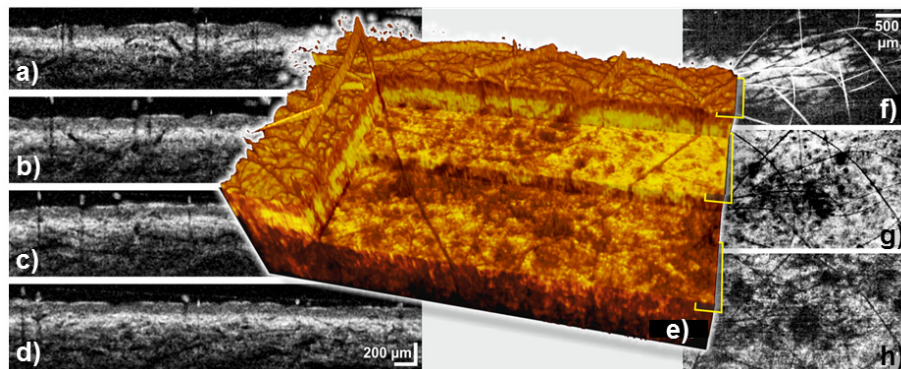


Fig. 4. Images of pigmented thin skin taken using the partially integrated SD-OCT system. (a-c) Cross-sectional views of a three-dimensional volume obtained at a location with increased melanin concentration. (f-h) *En face* views at different depths. (e) Three-dimensional volume-rendered representation of OCT image data. The yellow markers delineate the corresponding positions of the *en face* views.

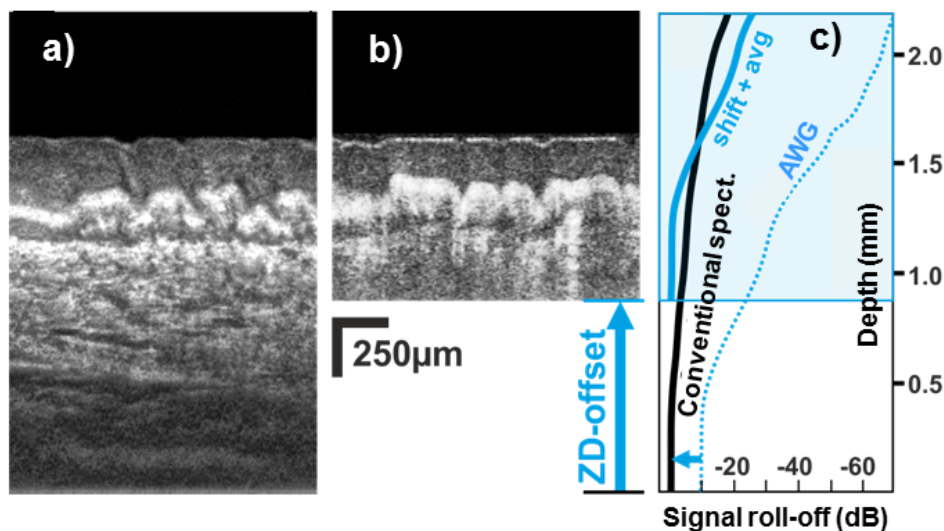


Fig. 5. Cross-sectional tomograms of the scar tissue at the index finger. Images taken with $32 \times$ average using (a) the 1300-nm custom-designed SD-OCT system and (b) the partially integrated SD-OCT system. For the latter image, the zero delay is offset (ZD-offset) by ~ 800 μm toward the region of interest to compensate for ~ 10 dB loss caused by signal roll-off. (c) The signal roll-off curves of the partially integrated OCT system using an AWG spectrometer (blue dashed line) and the custom-designed OCT system using a conventional spectrometer (black solid line). The resulting signal roll-off of the partially integrated OCT system after compensation is given by the blue solid line.

3.4 Current imperfections and possible improvements

The obtained volumetric images of human skin in multiple locations and subjects demonstrate that our partially integrated SD-OCT system with a $7.5\text{-}\mu\text{m}$ axial resolution, 1.4-mm depth range, and 74-dB SNR is capable of acquiring high-quality *in vivo* OCT images of human skin. Despite the fact that this is the first demonstration of *in vivo* imaging with an on-chip OCT system, the performance parameters come surprisingly close to a state-of-the-art bulk OCT system; nevertheless, there is significant room for improvement.

Though 74-dB SNR is sufficient for biomedical imaging, in principle it can be improved to 94 dB by diminishing the non-adiabatic-coupler loss from 2.5 dB to its theoretical limit of 0 dB with an optimized lithography and etching procedure, fiber-to-chip coupling losses from 3 dB to < 0.5 dB by spot-size converters [27], e.g. tapered input waveguides [28], objective-lens transmission loss from 1.5 dB to < 1 dB by use of near-infrared objective lenses, and AWG excess loss from 1.5 dB to < 0.5 dB by applying vertical tapers at the arrayed-waveguide/FPR interfaces [29].

The AWG and coupler were designed to operate at a 1250-nm center wavelength, whereas later a 1320-nm light source was chosen for the experiments, thereby degrading the coupler splitting ratio by 5%, while slightly improving the depth range by ~ 50 μm due to the longer operating wavelength, despite the reduced AWG-limited resolution of 0.29 nm.

At SiON/air interfaces, waveguides were tapered from 1.8 μm to 3 μm to efficiently couple light to the chip. The specific taper design caused a wavelength-dependent destructive interference, thereby reducing the 100-nm bandwidth of the light source to a usable bandwidth of 75 nm (with a Gaussian-like spectrum), consequently increasing the axial resolution in tissue from 5 μm to 7.5 μm . An improved taper design can avoid this effect.

The internal scattering caused by waveguide surface roughness and back-reflections at SiON/air interfaces resulted in enlarged background in the measurements, which limits the usable dynamic range of the detector. Polishing the waveguide facets at an 8° angle reduced,

albeit could not eliminate these back-reflections. Scattering can be diminished with a higher-quality e-beam mask and optimized etching procedure.

The AWG spectrometer and the splitters support both polarization states, which makes them suitable for polarization-sensitive OCT applications as well. The non-degeneracy of the TE and TM modes of the on-chip splitter can be determined by the differential group delay (which is the relevant polarization-mode-dispersion related quantity for optical waveguides) of the tapered optical waveguides which was calculated to be 6 μs (length = 3.5 mm). This number can be optimized by controlling the material and waveguide birefringence in accordance with the need of the OCT system.

4. Conclusions

In vivo imaging with a partially integrated SD-OCT system has been demonstrated by acquiring volumetric images of human skin in multiple locations and subjects. In-tissue axial resolution of 7.5 μm and in-tissue depth range of 1.4 mm was achieved. Current performance of the partially integrated OCT system can be further improved to the level of bulky commercial OCT systems with an optimized design and high-quality fabrication facilities. Considering the ability of lithography to mass-produce optimized optical systems, full on-chip integration of a complete OCT instrument will ultimately allow for significantly lower fabrication costs and pave the road toward a much wider distribution of OCT systems and new fields of applications.

Acknowledgments

This work was financially supported by the Smart Mix Program of the Netherlands Ministry of Economic Affairs and the Netherlands Ministry of Education, Culture and Science, Medical University Vienna, and the European Union projects FUN OCT (FP7 HEALTH, contract no. 201880) and FAMOS (FP7 ICT, contract no. 317744). The authors thank Anton Hollink, Henk van Wolferen, Milorad Jevremovic, Bernhard Rosenauer, and Angelika Unterhuber for technical support, Gabriel Sengo for device fabrication, Dimitri Geskus and XiOPhotonics for angle-polishing the device, Gunay Yurtsever and Alfred Driessen for fruitful discussions, and the Vereniging voor Biofysica en Biomedische Technologie for providing a travel grant.